A COMPARISON OF URANS AND LES FOR SOOT PREDICTIONS IN AN AERO-ENGINE MODEL COMBUSTOR

C. Eberle
Institute of Combustion Technology
German Aerospace Center (DLR)
Paffenwaldring 38-40
70569 Stuttgart, Germany
christian.eberle@dlr.de

P. Gerlinger
Institut für Verbrennungstechnik
der Luft- und Raumfahrt
University of Stuttgart
70569 Stuttgart, Germany

M. Aigner
Institute of Combustion Technology
German Aerospace Center (DLR)
Paffenwaldring 38-40
70569 Stuttgart, Germany

Abstract

This paper presents time-resolved numerical simulations of a well-characterized aero-engine model combustor. Recently published unsteady Reynolds averaged Navier-Stokes simulations (URANS) are compared to large eddy simulations (LES). Finite-rate chemistry, where a separate transport equation is solved for each chemical species, is employed for the gas phase, a sectional approach for PAHs, and a two-equation model for soot. Thus feedback effects such as the consumption of gaseous soot precursors by growth of soot and PAHs are inherently captured accurately. The numerical results (velocity components, temperature and soot volume fraction) compare well with experimental data. No significant differences between URANS and LES are found for time-averaged velocity components and time-averaged temperature, while the prediction of the soot distribution was significantly improved by LES. It will be shown that accurate description of the instantaneous flame structure, especially the hydroxyl distribution, by resolution of turbulent scales is of fundamental importance for accurate soot predictions in the present test case.

1. INTRODUCTION

1.1. Motivation

Combustion is one of the oldest heat and power generation technologies and continues to play an important role in covering the energy demand of the world. The intense use of combustion, however, has led to several environmental issues, such as soot emissions. Soot and soot precursors are suspected to be carcinogenic. Furthermore, soot from aircraft engines is suspected to increase cirrus clouds at high altitudes and thus has an impact on the climate [28, 45, 46, 29]. From an engineering point of view, soot indicates incomplete and hence less efficient combustion. By its high radiative emissivity, soot also contributes to locally elevated heat loads on combustion chamber walls [33, 32, 43]. Therefore, continuous efforts are made to reduce the soot emissions of combustion systems. Soot models provide a detailed insight into soot evolution processes and are thus an essential tool for the optimization of combustion devices.

Different soot models have been reported in literature. On one hand, these models can be distinguished by their soot nucleation mechanism. In simple nucleation models, soot is directly formed from acetylene [35, 52, 59, 15] while in more complex nucleation models benzene [35, 59], naphthalene [8] or pyrene [50, 3, 12, 36] are used as incipient species. These complex models thus take into account the slow chemistry of polycyclic aromatic hydrocarbons (PAHs), however, at a significant increase of computational cost. An alternative approach is the definition of somehow lumped PAH species [56, 10, 5, 30, 42] to efficiently model the dominant chemical processes of PAH evolution.

On the other hand different techniques for the statistical approximation of the soot size distribution were developed. One of the most basic techniques are two-equation models, where soot is described by two independent variables, e.g. soot mass fraction and soot particle number density [34, 60, 26, 52]. In two-equation models, a monodisperse soot particle size distribution and spherical soot particles are assumed. In contrast to more elaborate models which consider polydisperse soot particle size distributions, as discussed below, two equation models usually predict fewer particles with larger diameters. Accurate predictions of soot volume fractions can be achieved, however. Due to their computational efficiency, two-equation models are widely used for simulation of complex combustion devices such as aero-engines [10] or internal combustion engines [16]. A more detailed statistical approximation of the soot size distribution is given by the method of moments [18, 15, 11, 42], where transport equations for moments of the soot size distribution are solved. A Langrangian scheme to solve these transport equations was recently developed by [2]. In sectional approaches [50, 56, 8, 12, 5, 36], the soot size

distribution is discretized into bins, which can be treated in analogy to chemical species. Monte Carlo simulations are also used to predict soot size distributions [40, 41].

Due to its computational efficiency, a two-equation model which provided promising results in previous simulations of complex three-dimensional configurations [6, 10, 13, 14] is applied in the present work. In contrast to classical implementations of two-equation soot models with acetylene based soot inception [34], we include PAHs which are described by a sectional approach and model soot inception by PAH growth reactions.

1.2. Selection of Validation Experiment

For complex combustion systems, e.g. aero-engine combustors, quantitative validation of soot models is difficult since most experimental investigations of soot from real aero engine combustors are limited to measurements of the smoke number at the combustor exit [42, 13]. They lack information concerning the spatial distribution of soot as well as particle size distributions. Soot information from inside the combustor is still more rare. So far detailed validation data for sooting combustion was restricted to academic test cases like laminar flames [53, 38, 1, 23, 58, 61, 51, 17] or turbulent jet flames [49, 30] which offer full optical access for application of non-intrusive measurement techniques. Until recently, there were no test cases available which provide well-defined boundary conditions and comprehensive validation data on one hand and on the other hand feature technically relevant conditions as confined swirling flow and operation at elevated pressure.

This gap was closed by Geigle et al. [20, 21, 22] and Stöhr et al. [57] who performed measurements yielding a detailed characterization of an aero-engine model combustor. Optical access to the combustion chamber via four quartz windows permitted the use of non-intrusive laser measurement techniques. This new data set provides an unprecedented opportunity to validate soot models at technically relevant conditions, burning ethylene instead of the more complex realistic fuel kerosene. In this way the problem of spray modeling and the choice of accurate spray initial conditions are avoided. A significant improvement of the present experiment compared to an earlier configuration [31], which was also used for soot model validation [9], is the separate control of the swirled primary air inflows. Furthermore the geometry of the secondary air inlets was optimized and more comprehensive validation data is available.

1.3. Numerical Solution Approach

Soot modeling in turbulent combustion is a complex task involving various fields of research, i. e. gas phase and soot chemistry, turbulence, chemistry-turbulence interaction and heat radiation must be considered in order to accurately predict soot. Due to high computational cost, the simultaneous use of the most accurate modeling approach in any of the mentioned fields is often not feasible but a compromise between available computational resources and required accuracy must be found.

In previous work, we therefore investigated the applicability of an efficient turbulence modeling approach, namely URANS, for soot predictions at technically relevant conditions [14]. The URANS results showed good agreement to measurements in terms of time-averaged velocity components and time-averaged temperature; also a precessing vortex core was resolved in accordance to experimental investigations [57]. However, deviations between measured and calculated soot distributions were observed and it was claimed that these deviations partially result from limitations of URANS, especially, it was argued that scale resolving simulations such as LES are required to more accurately describe the instantaneous OH distribution and ultimately achieve better agreement between measured and predicted soot distributions in the present test case. For confirmation, LES were performed and are compared to recently published URANS [14].

As no dominant influence of subgrid scale chemistry turbulence interaction (sgs-TCI) was observed in previous simulations of a confined, swirl stabilized flame and good results were obtained by assuming sgs-TCI to be small and thus linear [37], this assumption is also taken in the present work. For the sake of computational efficiency, soot is described by a two-equation model [10, 6]. All simulations use the in-house code THETA (Turbulent Heat Release Extension of TAU) [9]. THETA is a parallelized, unstructured finite volume solver which is optimized for gas turbine related combustion problems.

2. GOVERNING EQUATIONS AND NUMERICAL SCHEME

The averaged and modeled equations for conservation of mass and momentum read:

$$\frac{\partial \overline{\rho}}{\partial t} + \frac{\partial \overline{\rho}\widetilde{u_i}}{\partial x_i} = 0 \ , \tag{1}$$

$$\frac{\partial \overline{\rho}\widetilde{u_i}}{\partial t} + \frac{\partial \overline{\rho}\widetilde{u_i}\widetilde{u_j}}{\partial x_j} + \frac{\partial \overline{p^*}}{\partial x_i} - 2\frac{\partial}{\partial x_j}\left((\mu+\mu_t)\left(\widetilde{S}_{i,j} - \frac{1}{3}\widetilde{S}_{k,k}\delta_{i,j}\right)\right) = \overline{\rho} g_i \ . \tag{2}$$

The overbars $\overline{\phi}$ and $\widetilde{\phi}$ denote Reynolds and Favre averages in the URANS context and respective filtering operations in the LES context. The Einstein summation convention is applied here and in the following. u_i is the velocity component in x_i-direction, ρ the density, μ the molecular viscosity, μ_t the turbulent viscosity, $S_{i,j}$ the strain tensor and g_i the gravity constant in x_i-direction. The pseudo-pressure p^* is defined as

$p^* = p + \frac{2}{3}\rho k \delta_{ij}$, where p is the pressure, k the turbulent kinetic energy and δ_{ij} the Kronecker delta. In case of URANS, the turbulent viscosity is calculated by the two-equation shear stress transport (SST) turbulence model [39] and in case of LES by the zero-equation wall adapting local eddy viscosity model (WALE) [44]. The filtered and modeled transport equations of specific enthalpy h (h is defined as the sum of thermal and chemical enthalpy: $h = \int_{T_0}^{T} c_p \, \mathrm{d}T + \sum_\alpha \Delta h^0_{f,\alpha}$, where $\Delta h^0_{f,\alpha}$ is the standard enthalpy of formation) and reactive scalars Y_α (including mass fractions of gaseous and PAH species, soot mass fraction Y_s and soot particle number density n_s, see section 3) read:

$$\frac{\partial \overline{\rho}\widetilde{h}}{\partial t} + \frac{\partial \overline{\rho}\widetilde{u_i}\widetilde{h}}{\partial x_i} - \frac{\partial}{\partial x_i}\left(\left(\frac{\lambda}{c_p} + \frac{\mu_t}{\mathsf{Pr}_t}\right)\frac{\partial \widetilde{h}}{\partial x_i}\right) = \widetilde{\omega}_h \ , \quad (3)$$

$$\frac{\partial \overline{\rho}\widetilde{Y}_\alpha}{\partial t} + \frac{\partial \overline{\rho}\widetilde{u_i}\widetilde{Y}_\alpha}{\partial x_i} - \frac{\partial}{\partial x_i}\left(\left(\frac{\mu}{\mathsf{Sc}} + \frac{\mu_t}{\mathsf{Sc}_t}\right)\frac{\partial \widetilde{Y}_\alpha}{\partial x_i}\right) = \widetilde{\omega}_\alpha \ , \quad (4)$$

where λ is the thermal conductivity, c_p the specific heat at constant pressure, $\mathsf{Pr}_t = 0.7$ the turbulent Prandtl number, and Sc and $\mathsf{Sc}_t = 0.7$ the laminar and turbulent Schmidt number, respectively. For the soot properties Y_s and n_s, molecular diffusion is neglected ($1/\mathsf{Sc} = 0$) due to the large Schmidt number of soot particles , while for other reactive scalars $\mathsf{Sc} = 0.7$ is assumed. The source terms ω_h and ω_α describe heat radiation and consumption as well as production of reactive species due to chemical reactions, respectively.

2.1. Heat Radiation

Assuming an optically thin medium, the heat radiation source term reads:

$$\omega_h = -4 \ \sigma_S \ \rho \ \epsilon_s(T) \ \ Y_s \ T^4 \ , \quad (5)$$

where σ_S is the Stefan-Boltzmann constant. The emissivity coefficient for soot, $\epsilon_s(T)$, is derived from the work of Di Domenico et al. [10] as

$$\epsilon_s(T) = \frac{c_s}{\rho_s} \ T, \quad (6)$$

with the constant $c_s = 441 \frac{1}{Km}$ and the soot density $\rho_s = 1800 \frac{kg}{m^3}$. In the present work interaction between turbulence and heat radiation is assumed to be linear. Taking this assumption, the filtered heat radiation source is thus given by $\widetilde{\omega}_h = \omega_h(\widetilde{Y}_s, \widetilde{T})$. The radiation model was validated in previous work [10, 5, 30].

2.2. Chemical Source Term

The chemical source term ω_α is described by a finite-rate combustion model where a separate transport equation is solved for each reactive scalar α. With the general form of a chemical reaction r,

$$\sum_{\alpha=1}^{N_{sp}} \nu'_{\alpha,r} \ \alpha = \sum_{\alpha=1}^{N_{sp}} \nu''_{\alpha,r} \ \alpha \ , \quad (7)$$

where ν are stoichiometric coefficients and N_{sp} the number of species and the source of a reaction r,

$$\omega_r = k_{f,r} \prod_{\beta=1}^{N_{sp}} C_\beta^{O'_{\beta,r}} - k_{b,r} \prod_{\beta=1}^{N_{sp}} C_\beta^{O''_{\beta,r}} \ , \quad (8)$$

the compact notation of the chemical source term ω_α is written as:

$$\omega_\alpha = M_\alpha \sum_{r=1}^{N_r} \left(\nu''_{\alpha,r} - \nu'_{\alpha,r}\right) \omega_r \ . \quad (9)$$

M_α is the molar mass of species α, N_r the number of reactions, and O the reaction order, respectively. $C_\beta = \rho Y_\beta / M_\beta$ is the concentration of species β. k_f and k_b are forward and backward rate coefficients which are modeled by Arrhenius equations. As discussed in section 1.3, sgsTCI is assumed to be linear. The filtered chemical source term is thus given by:

$$\widetilde{\omega}_\alpha = \omega_\alpha(\hat{T}, \hat{\boldsymbol{Y}}) \ . \quad (10)$$

A great challenge for finite-rate combustion models is the stiffness of the system of discretized transport equations which is induced by the high disparity of chemical time scales [24]. To mitigate the resulting time step limitation, an implicit discretization of the chemical source term is applied:

$$\boldsymbol{\omega}\left(\boldsymbol{\Phi}^{t+1}\right) = \boldsymbol{\omega}\left(\boldsymbol{\Phi}^{t}\right) + \frac{\partial \boldsymbol{\omega}}{\partial \boldsymbol{\Phi}}\left(\boldsymbol{\Phi}^{t+1} - \boldsymbol{\Phi}^{t}\right) \ , \quad (11)$$

where $\boldsymbol{\Phi}$ is the vector of reactive scalars and the averaging operator $\widetilde{(\ )}$ is dropped for clarity. The Jacobian $\boldsymbol{J} = \partial\boldsymbol{\omega}/\partial\boldsymbol{\Phi}$ is formulated analytically, which is more accurate and also more efficient than a numerical formulation [25].

3. GAS PHASE CHEMISTRY AND SOOT MODEL

The kinetics of gas phase species are modeled by a reaction mechanism which describes the formation of aromatic hydrocarbons up to benzene and toluene and has been validated for the combustion of small hydrocarbons, such as methane or ethylene at atmospheric and high-pressure conditions [55, 54]. The mechanism consists of 43 species and 304 reactions.

In our PAH and soot models [10, 5], all chemical reactions involving soot and PAHs are formulated in Arrhenius form and thus are compatible to chemical reactions of gas phase species. Hence, the transport equations

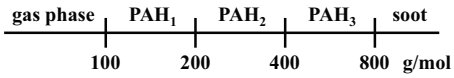

Figure 1: Distribution of PAH bins.

stemming from the PAH and soot models are solved by the finite-rate chemistry solver in the same way as the transport equations of gas phase species, thereby allowing a full coupling between soot, PAHs and the thermochemical state of the gas phase. Feedback effects of soot and PAHs on the gas phase such as consumption of gaseous soot precursors (predominantly acetylene, benzene and toluene) as well as heat radiation are thus inherently captured accurately.

PAHs are modeled by a sectional approach, where, as illustrated by Fig. 1, aromatic species with a molar mass between 100 and 800 g/mol are discretized by three bins with a logarithmic scaling factor of two. PAH chemistry is divided into four sub mechanisms: PAH formation, C_2H_2 condensation, PAH collisions and PAH oxidation. The PAH model was derived in detail by Blacha et al. [5], thus only a brief overview is given in this paper. PAH formation, or rather interaction between gas phase and PAH_0 in general, is modeled by 19 reversible reactions derived from the detailed reaction mechanisms by Richter et al. [50] and Slavinskaya et al.[54]. An example is the reaction $C_7H_7 + CH_2 = A1C_2H_3 + H$, where styrene is replaced by (ν PAH0) and the stoichiometric coefficient ν is calculated from conservation of mass. For the full list of reactions and reaction rate parameters, the reader is referred to the work of Blacha et al. [5].

PAH growth is described by the HACA (hydrogen abstraction - acetylene addition) mechanism [19] and by PAH collisions,

$$\mathrm{PAH}_k + \mathrm{PAH}_j \rightarrow \nu_1'' \ \mathrm{PAH}_k + \nu_2'' \ \mathrm{PAH}_{k+1} + \nu_{\mathrm{H_2}}'' \mathrm{H_2}, \tag{12}$$

with $j \leq k$, where for $k = 3$, PAH_{k+1} is replaced by soot. All PAH growth reactions which involve the last PAH bin as reactant therefore describe soot inception. The rate of reaction (12) is determined by the kinetic theory of gases using a constant collision efficiency $\gamma_{k,j} = 0.3$. Following Pope et al. [47] stoichiometric coefficients are calculated depending on intra sectional distribution functions and atom conservation. Regarding PAH oxidation, the two oxidants OH and O_2 are considered.

A two-equation model is applied for soot where the evolution of the soot aerosol is described by the soot mass fraction Y_s and the soot particle number density n_s. The soot model considers soot surface growth by acetylene condensation, collisions between soot and PAHs, coagulation and soot oxidation by OH and O_2. Soot formation is captured by the PAH model since PAH growth reactions involving the last PAH bin as educt yield to soot nucleation.

A detailed derivation of our implementation of the two-equation soot model is given by [10] and [6]. Due to the high complexity of soot evolution processes and the resulting modeling uncertainties, comprehensive validation of soot models is of fundamental importance. The soot model was thus applied to both laminar and turbulent combustion including different fuels from methane to Jet-A1 surrogates. Using the same set of model constants for all simulations, a good overall agreement with experiments has been reported [5, 4, 30].

4. RESULTS

4.1. Investigated Test Case

4.1.1 Combustor Configuration

The set-up of the aero-engine model combustor is illustrated in Fig. 2. The nozzle is fed by three concentric flows. Air at room temperature is injected through a central nozzle (diameter 12.3 mm) and an annular nozzle (inner diameter 14.4 mm, outer diameter 19.8 mm). Both air flows are fed from separate pleni and pass radial swirlers. The swirler of the central air consists of 8 channels and the swirler of the annular air of 12 channels. Gaseous fuel (ethylene) is injected between the co-swirling air flows through 60 straight channels (0.5×0.4 mm^2). The fuel channels, which are resolved by the CFD grid, form a concentric ring and mimic the atomizing lip for spray combustion in aero-engine combustors (cf. Fig. 2(b)). The combustion chamber measures 120 mm in height and has a square cross section of 68×68 mm^2 with beveled edges. Four quartz windows (height 127 mm, width 59 mm) provide excellent optical access of the flame. Secondary air is injected from the four corners of the combustion chamber through ducts with 5 mm diameter at a height of 80 mm (cf. Fig. 2(a)). More details about burner configuration, test rig and experimental setup are given by Geigle et al. [20].

4.1.2 Validation Data

Several operating conditions have been investigated experimentally. Starting from a 3 bar reference operating point with a primary equivalence ratio of $\phi = 1.2$ and a thermal power of $P \approx 30$ kW, parameter variations were performed to study the influences of secondary air injection, pressure, thermal power, split between central and annular air and the equivalence ratio, respectively, on the soot distribution. Comprehensive validation data obtained by several laser diagnostics (velocity components by stereo-PIV (particle image velocimetry), temperature by CARS (coherent anti-Stokes Raman scattering) and soot volume fraction by LII (laser-induced incandescence)) is available for each operating point [20, 21, 57]. In this paper, simulations of the 3 bar reference operating point are presented. The corresponding inflow mass fluxes, hydraulic diameter based Reynolds

Inflow	mass flux [g/s]	Re/1000	T [K]
Ring air	7.08	15	293
Central air	3.03	17	293
Secondary air	4.04	14	293
Fuel C_2H_4	0.83	-	297

Table 1: Operating point parameters. Reynolds numbers are based on the respective hydraulic diameter.

numbers, and temperatures are listed in Tab. 1.

4.2. Simulation Details

The simulations were performed on a three-dimensional fully tetrahedral grid with 6.6 million points corresponding to 36.5 million tetrahedra. The computational domain is shown in Fig. 2. The inflow boundaries are placed well upstream of the swirlers. To take heat losses into account, isothermal walls are assumed. Estimated wall temperatures based on thermocouple measurements amount to 350 K for the swirlers, 600 to 700 K for the combustion chamber and 900 K for the windows. Special attention has been paid to properly resolve the mixing of fuel and air. To this end, the mesh was locally refined in the vicinity of the fuel channels to a spatial resolution of $\Delta x = \sqrt[3]{V_{\text{cell}}} \approx 0.05$ mm (cf. Fig. 2(b)). The resolution in the region of flame stabilization is 0.25 mm, while 0.5 mm are applied in the majority of the computational domain and 1.0 mm towards the outlet passage.

Appropriate second order discretization schemes are used in space and time. To ensure convergence, a time step width of 0.5 μs was applied. Pressure-velocity coupling is realized by a projection method [7]. In total, 55 transport equations are solved (five equations for momentum, pressure correction and specific enthalpy, two equations for turbulence modeling (only in case of URANS), 43 equations for gas phase species, and five equations for PAHs and soot, respectively). Statistics were sampled over a physical time of approximately 60 ms, which corresponds to about six flow through times. One simulation took about 55 days on 256 cores ($\approx$ 338 000 CPU hours on Intel Xeon X5570 quad-core processors with a clock rate of 2.93 GHz).

4.3. Global Grid Resolution Criteria

To evaluate to quality of an LES in terms of grid resolution, two global criteria (in contrast to local criteria such as spectra or two-point correlations) are commonly used. Pope [48] proposed that the ratio between resolved and total turbulent kinetic energy should exceed at least 80 %, to properly resolve turbulent scales down to the inertial range. However, based on experience, this criterion is required but often not sufficient. In the present work, therefore, the ratio of turbulent viscosity to molecular viscosity,

$$r_\mu = \left\langle \frac{\mu_t}{\mu} \right\rangle \ , \tag{13}$$

where $\langle \ . \ \rangle$ denotes temporal averaging, is used to evaluate to quality of the LES. This ratio should be of order 10 or less (and thus orders of magnitude lower compared to URANS) to sufficiently resolve turbulent scales [27]. Time-averaged and instantaneous viscosity ratios are shown in Fig. 3. Except for some regions in the inner swirler, both, the time-averaged and the instantaneous viscosity are significantly smaller than 10, indicating a sufficient resolution of turbulent scales by the CFD grid.

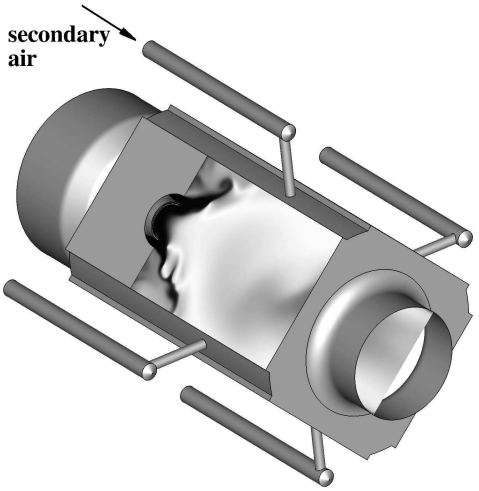

(a) Computational domain.

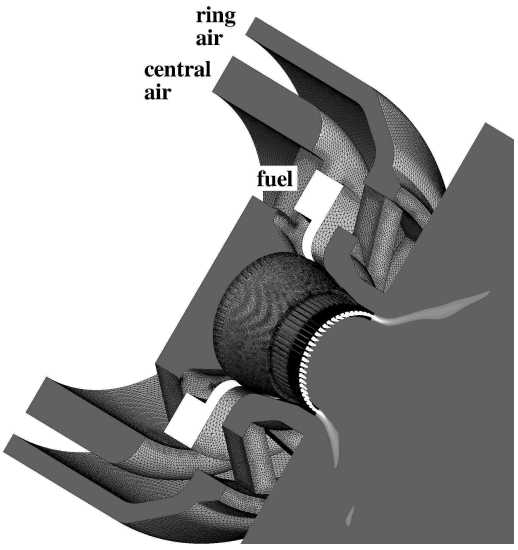

(b) Injection system.

Figure 2: The aero-engine model combustor. a) Computational domain with calculated temperature. b) Detailed view of the injection system with calculated C_2H_4 mass fraction.

4.4. Velocity Field

Figure 4 shows streamlines of representative calculated instantaneous flow fields. Dominant features of the turbulent swirling flame are the inner and outer recirculation zones (IRZ and ORZ) which provide heat and radicals for flame stabilization.

Since URANS relies on statistically averaged equations, the calculated velocity field displayed in Fig. 4(a) is per model definition smoother than the true turbulent field. As discussed in previous work [14], and as indicated by the black lines in Fig. 4(a), URANS however predicts the dominant deterministic motion in the present test case, which is a three-dimensional helical vortex structure in the inner shear layer (ISL), frequently termed precessing vortex core (PVC), at a frequency of 500 Hz. LES on the other hand resolves a certain range of turbulent scales and is thereby able to predict significantly more complex flow patterns as shown in Fig. 4(b).

A comparison between calculated and measured axial velocity profiles is given in Fig. 5. Profiles at the axial positions x = 4, 12, 45, and 95 mm are selected as representative for the flame, including the inflow region with strong reaction and the post-quench zone. At x = 4 mm and x = 12 mm the flow field is characterized by velocity peaks between the outer and inner shear layer and a pronounced inner recirculation zone. At the cited axial positions, the calculated velocity peaks are sharper compared to the experiment, thus the width of the inner recirculation zone (IRZ) is slightly overpredicted. Also, the maximium negative axial velocity in the IRZ is higher compared to the experiment, especially in case of URANS. Good to excellent agreement is observed at x = 45 mm where the velocity distribution is more homogeneous and the velocity peaks close to the combustion chamber walls are not captured by the measurements due to limited optical access. The central velocity plateau which develops downstream of secondary air injection is captured well by both, LES and URANS. Overall, LES performs slightly better than URANS as it better predicts the maximum negative axial velocity at the most upstream position. However, no major differences in terms of time-averaged axial velocity are found between URANS and LES.

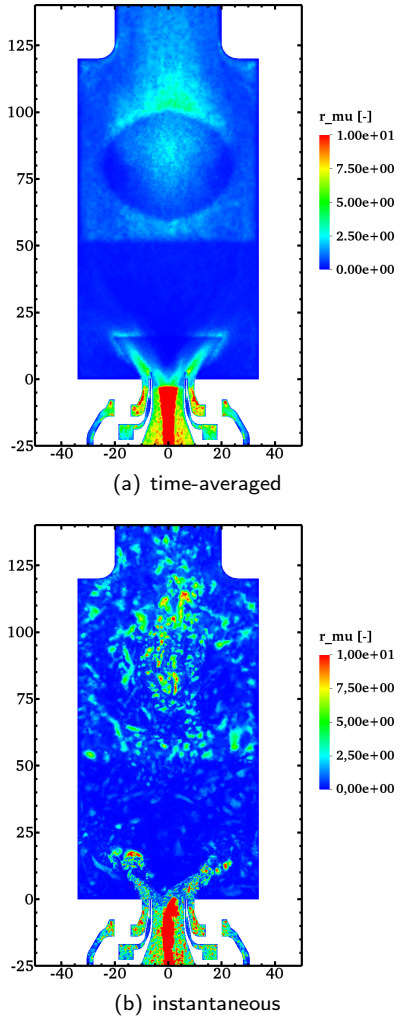

Figure 3: Ratio of turbulent to molecular viscosity r_μ: (a) LES, time-averaged. (b) LES, instantaneous. Dimensions are in mm.

4.5. Temperature

Measured and calculated temperatures are compared in Fig. 6, where radial profiles at the axial positions x = 1, 12, 45, and 95 mm are shown. At the most upstream position (x = 1 mm), measurements and LES show cold gas in the IRZ, while recirculating hot gas is present in the ORZ. The URANS results however, as a result of the overpredicted negative axial velocity as shown in Fig. 5(d), show hot gas in the IRZ. Furthermore, URANS underpredicts the temperature in the ORZ.

At x = 12 mm hot gas penetrates the IRZ and low temperatures are observed only between the inner and the outer shear layer. In line with the most upstream position, URANS overpredicts the width of the central hot temperature plateau and underpredicts the temperature in the ORZ. LES performs better in the cited regions, however it overpredicts the temperature between the inner and outer shear layer. Taking into account that accurate temperature predictions in the region of flame stabilization are highly challenging and the high complexity of the present test case, good to reasonable agreement between simulation and experiment is found.

Excellent agreement between measurements and simulation at x = 45 mm, where a homogeneous temperature profile indicates completely burnt mixture, and in the post-quench region (x = 95 mm) shows that heat losses due to radiation and isothermal walls are well described. Again, no significant differences are observed between URANS and LES.

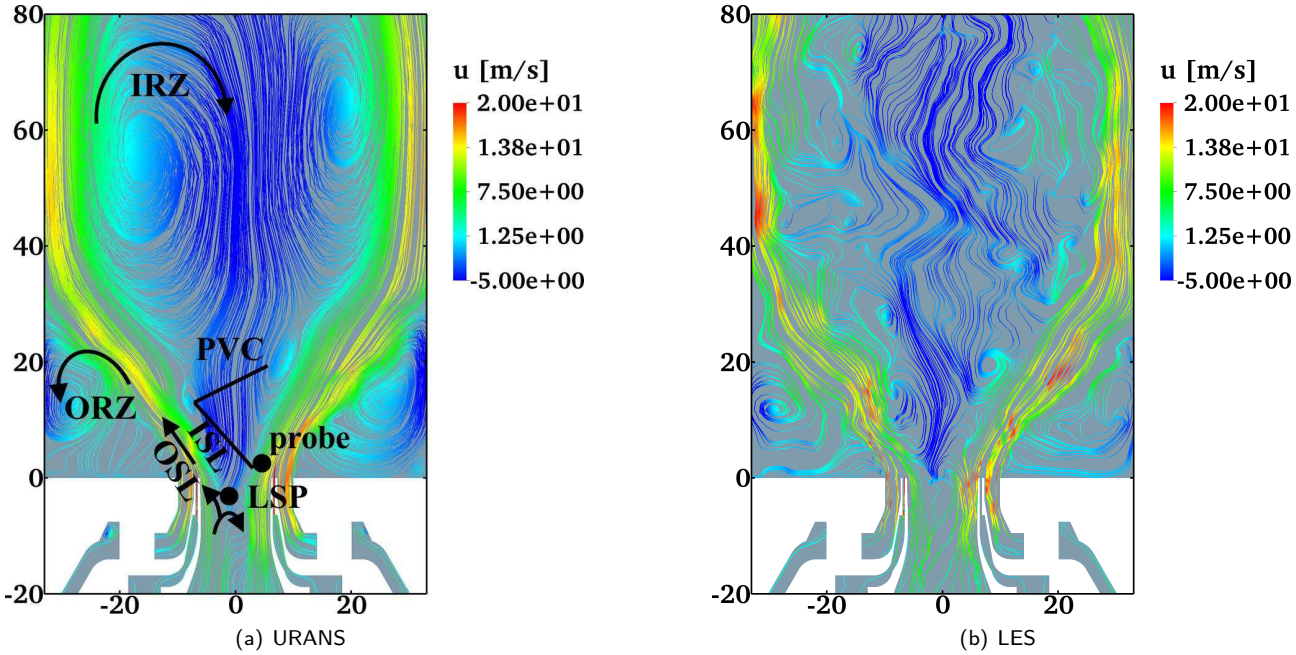

(a) URANS (b) LES

Figure 4: Streamline plots of representative calculated instantaneous flow fields. (a) URANS (b) LES Dimensions are in mm.

4.6. Soot volume fraction

Measured and calculated distributions of the soot volume fraction f_v are shown in Fig. 7. As discussed in detail by Eberle et al. [14], there are three characteristic differences between the measured soot volume fraction distribution and the URANS results. Firstly, the maximum soot volume fraction ($f_{v,max}$ = 0.54 ppm) is higher compared to the experiment ($f_{v,max}$ = 0.037 ppm). This applies also to LES ($f_{v,max}$ = 0.64 ppm) since the same soot model was applied for both, URANS and LES. Possible reasons are discussed in previous work [14]. Secondly, soot is oxidized to fast. In both simulations, soot is completely oxidized downstream of an axial position of approximately 70 to 75 mm. This is in contrast to the measurements where soot is observed as far as 110 mm downstream of fuel injection. The afore-discussed overprediction of soot volume fractions has two implications on soot oxidation: Firstly, soot precursors such as acetylene and PAHs are consumed too quickly and can hence not balance soot oxidation by further contributing to soot growth at more downstream positions. Secondly, the oxidation rates are too high since they are proportional to the soot concentration, which is overpredicted. Finally, in contrast to measurements, URANS does not predict soot on the axis of the combustion chamber close to the stagnation point between IRZ and inflow, whereas LES does accurately predict the shape of the soot distribution in this region.

To better understand these significant differences between URANS and LES, Fig. 8 shows plots with instantaneous mass fractions of O_2 and OH. Isolines of acetylene mass fraction and soot volume fraction are given as well. It is important to note that URANS, in contrast to simultaneous LII and OH-PLIF measurements by Geigle et at. [21], predicts high hydroxyl concentrations on the center line of the combustor at any given instant in time (as shown by time-resolved analysis in [14]) thereby preventing soot on the center line due to the oxidative potential of OH. This persistent prediction of hydroxyl in the cited region is attributed to the limitations URANS, which only resolves deterministic transient motion. LES, however, more accurately describes the instantaneous flame structure by resolving turbulent scales and subsequently predicts, in agreement to measurements [21], zones with low OH concentrations, which are filled with soot, while overlapping of soot and OH is minor.

5. CONCLUSIONS AND OUTLOOK

URANS and LES of a well-characterized, confined, sooting swirl flame using a finite-rate chemistry model where a separate transport equation is solved for each species were performed successfully. Velocity components and temperature are predicted with good to excellent agreement against measurements and reasonable agreement was found for soot.

While no significant differences between URANS and LES were observed for time-averaged axial velocity and temperature, the prediction of the shape of the soot distribution was significantly improved by LES due to a more accurate description of the instantaneous flame structure, i. e. the hydroxyl mass fraction. As future work, large-eddy simulations with an extended sectional soot model (including reversible soot precursor chemistry and a revised soot oxidation model) are planned to further

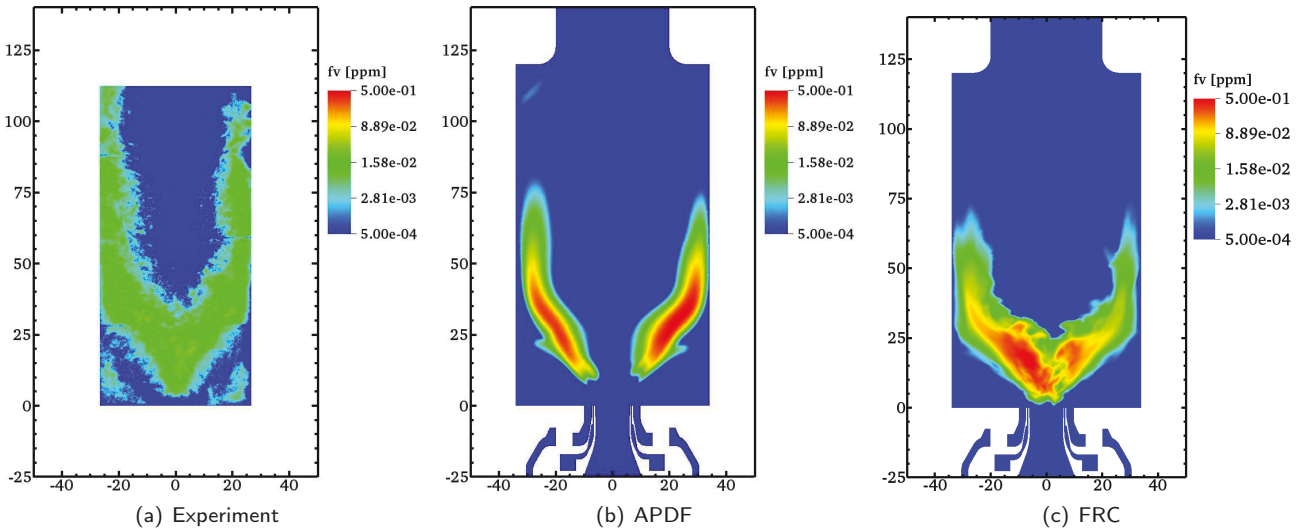

(a) Experiment (b) APDF (c) FRC

Figure 7: Predicted and measured time-averaged soot volume fraction f_v: (a) Measured f_v (b) Calculated f_v, URANS. (c) Calculated f_v, LES. Dimensions are in mm.

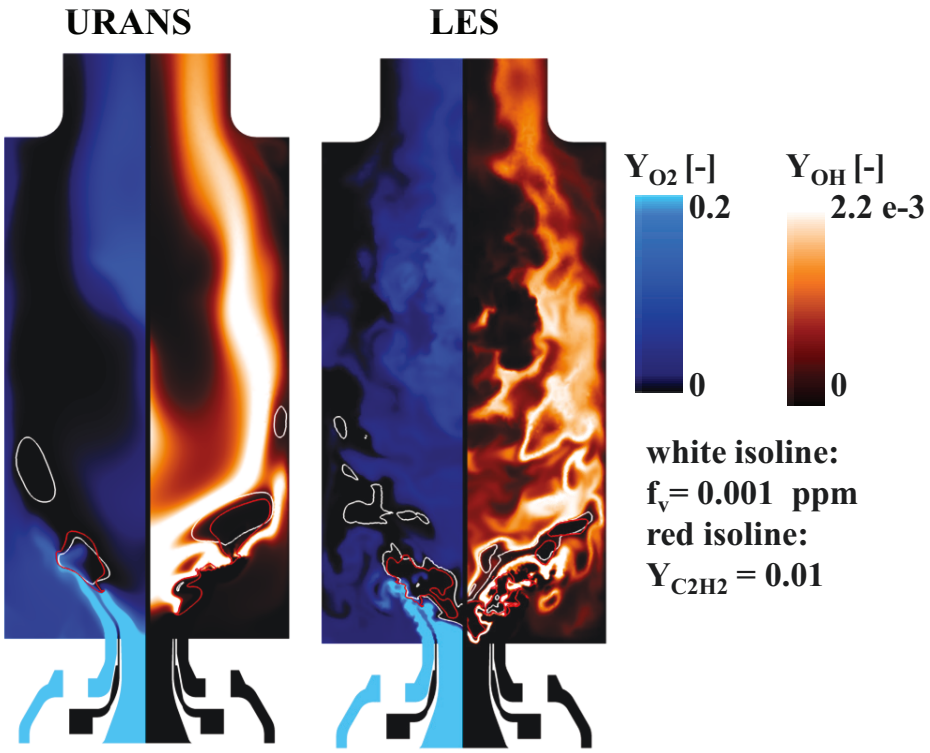

Figure 8: Instantaneous calculated distributions. Molecular oxygen mass fraction Y_{O_2} (left hand side of the respective plot) and hydroxyl mass fraction Y_{OH} (right hand side of the respective plot).

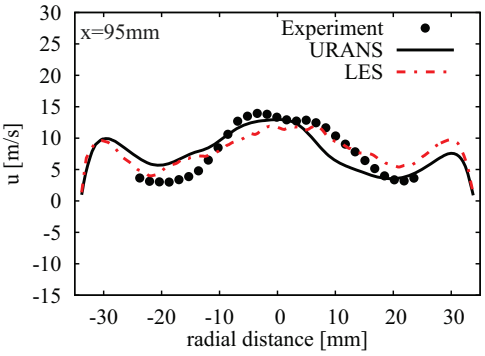

(a) x=95 mm.

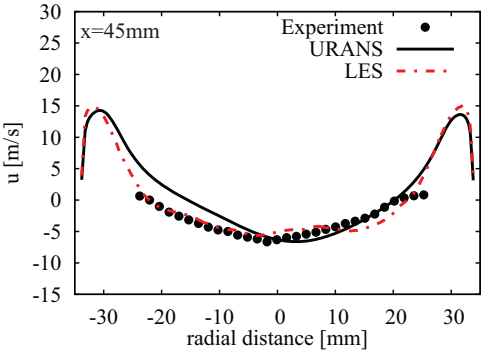

(b) x=45 mm.

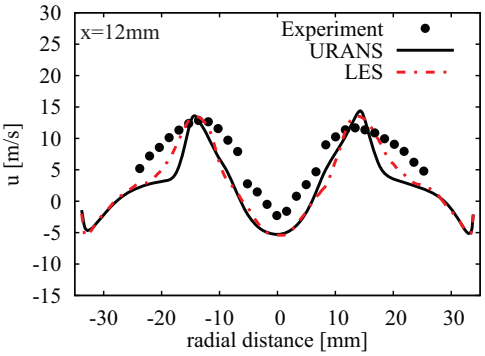

(c) x=12 mm.

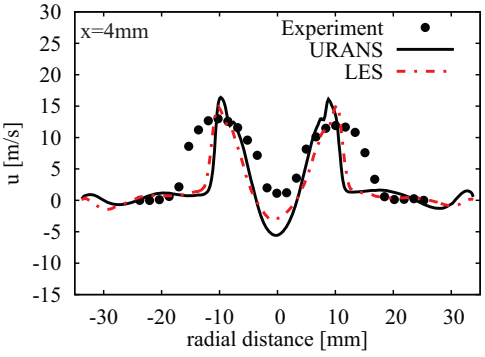

(d) x=4 mm.

Figure 5: Radial profiles of time-averaged axial velocity at selected downstream positions.

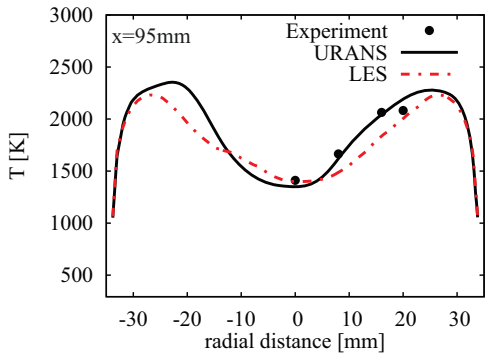

(a) x=95 mm.

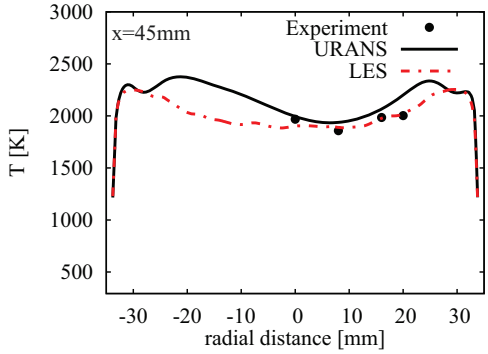

(b) x=45 mm.

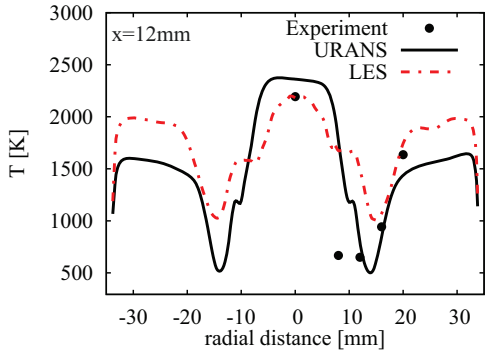

(c) x=12 mm.

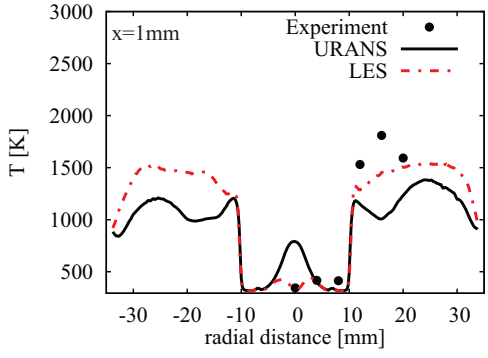

(d) x=1 mm.

Figure 6: Radial profiles of time-averaged temperature at selected downstream positions.

improve the prediction of soot with focus on maximum soot volume fraction and soot oxidation at technically relevant conditions.

ACKNOWLEDGMENTS

The authors thank K. P. Geigle and A. Fiolitakis for their contribution to this work and gratefully acknowledge the computing time granted by the John von Neumann Institute for Computing (NIC) and provided on the supercomputer JURECA at Jülich Supercomputing Centre (JSC). Part of this work was funded by the European Commission within the project Fuel Injector Research for Sustainable Transport (FIRST) under contract no. 265848.

REFERENCES

[1] Arana, C. P. ; Pontoni, M. ; Sen, S. ; Puri, I. K.: Field measurements of soot volume fraction in laminar partially premixed coflow ethylene/air flames. In: *Combustion and Flame* 138 (2004), S. 362–372

[2] Attili, A. ; Bisetti, F.: Application of a robust and efficient Lagrangian particle scheme to soot transport in turbulent flames. In: *Computers & Fluids* 84 (2013), S. 164–175

[3] Bhatt, J. S. ; Lindstedt, R. P.: Analysis of the impact of agglomeration and surface chemistry models on soot formation and oxidation. In: *Proceedings of the Combustion Institute* 32 (2009), S. 713–720

[4] Blacha, T.: *Effiziente Rußmodellierung in laminaren und turbulenten Flammen unterschiedlicher Brennstoffe*, Institute of Combustion Technology for Aerospace Engineering Universität Stuttgart, Diss., 2012

[5] Blacha, T. ; Di Domenico, M. ; Gerlinger, P. ; Aigner, M.: Soot predictions in premixed and non-premixed laminar flames using a sectional approach for PAHs and soot. In: *Combustion and Flame* 159 (2012), S. 181–193

[6] Blacha, T. ; Di Domenico, M. ; Rachner, M. ; Gerlinger, P. ; Aigner, M.: Modeling of soot and NO_x in a full scale turbine engine combustor with detailed chemistry. In: *Proceedings of the ASME Turbo Expo 2011: Power for Land, Sea and Air*, 2011

[7] Chorin, A. J.: Numerical solution of the Navier-Stokes equations. In: *Mathematics of Computation* 22 (1968), Nr. 104, S. 745–762. – ISSN 0025–5718

[8] D'Anna, A. ; Kent, J. H.: A model of particulate and species formation applied to laminar, nonpremixed flames for three aliphatic-hydrocarbon fuels. In: *Combustion and Flame* 152 (2008), S. 573–587

[9] Di Domenico, M.: *Numerical simulations of soot formation in turbulent flows*, Institute of Combustion Technology for Aerospace Engineering Universität Stuttgart, Diss., 2008

[10] Di Domenico, M. ; Gerlinger, P. ; Aigner, M.: Development and validation of a new soot formation model for gas turbine combustor simulations. In: *Combustion and Flame* 157 (2010), S. 246–258

[11] Donde, P. ; Raman, V. ; Mueller, M. E. ; Pitsch, H.: LES/PDF based modeling of soot-turbulence interactions in turbulent flames. In: *Proceedings of the Combustion Institute* 34 (2013), S. 1183–1192

[12] Dworkin, S. B. ; Zhang, Q. ; Thomson, M. J. ; Slavinskaya, N. A. ; Riedel, U.: Application of an enhanced PAH growth model to soot formation in a laminar coflow ethylene/air diffusion flame. In: *Combustion and Flame* 158 (2011), S. 1682–1695

[13] Eberle, C. ; Blacha, T. ; Gerlinger, P. ; Aigner, M.: Numerical simulations of soot and NO_x distributions in a full scale aero-engine combustor at two different flight altitudes. In: *Proceedings of the 52nd AIAA Aerospace Sciences Meeting*, 2014

[14] Eberle, C. ; Gerlinger, P. ; Geigle, K. P. ; Aigner, M.: Numerical investigation of transient soot evolution processes in an aero-engine model combustor. In: *Combustion Science and Technology* (2015)

[15] El-Asrag, H. ; Menon, S.: Large eddy simulation of soot formation in a turbulent non-premixed jet flame. In: *Combustion and Flame* 156 (2009), S. 385–395

[16] Farrace, D. ; Bolla, M. ; Wright, Y. ; Boulouchos, K.: Predicting in-cylinder soot in a heavy-duty diesel engine for variations in SOI and TDC temperature using the conditional moment closure model. In: *SAE Interational Journal of Engines* 6 (2013), S. 1580–1593

[17] Figura, L. ; Gomez, A.: Structure of incipiently sooting ethylene-nitrogen counterflow diffusion flames at high pressures. In: *Combustion and Flame* 161 (2014), S. 1587–1603

[18] Frenklach, M. ; Harris, S. J.: Aerosol dynamics modeling using the method of moments. In: *Journal of Colloid and Interface Science* 118 (1987), S. 252–261

[19] Frenklach, M. ; Wang, H.: Detailed mechanism and modeling of soot particle formation. In: Bockhorn, H. (Hrsg.): *Soot Formation in Combustion*. Springer Verlag, 1994

[20] Geigle, K. P. ; Hadef, R. ; Meier, W.: Soot formation and flame characterization of an aero-engine model combustor burning ethylene at elevated pressure. In: *Journal of Engineering for Gas Turbines and Power* 136 (2014), S. 021505–1–021505–7

[21] Geigle, K. P. ; Köhler, M. ; O'Loughlin, W. ; Meier, W.: Investigation of soot formation in pressurized swirl flames by laser measurements of temperature, flame structures and soot concentrations. In: *Proceedings of the Combustion Institute* 35 (2015), S. 3373–3380

[22] Geigle, K. P. ; O'Loughlin, W. ; Meier, R. H. W.: Visualization of soot inception in turbulent pressurized flames by simultaneous measurement of laser-induced fluorescence of polycyclic aromatic hydrocarbons and laser-induced incandescence, and correlation to OH distributions. In: *Applied Physics B, in press* (2015)

[23] Geigle, K. P. ; Schneider-Kühnle, Y. ; Tsurikov, M. S. ; Hadef, R. ; Lückerath, R. ; Krüger, V. ; Stricker, W. ; Aigner, M.: Investigation of laminar pressurized flames for soot model validation using SV-CARS and LII. In: *Proceedings of the Combustion Institute* 30 (2005), S. 1645–1653

[24] Gerlinger, P. ; Möbus, H. ; Brüggemann, D.: An implicit multigrid method for turbulent combustion. In: *Journal of Computational Physics* 167 (2001), S. 247–276

[25] Gerlinger, P. ; Stoll, P. ; Brüggemann, D.: An implicit multigrid method for the simulation of chemically reacting flows. In: *Journal of Computational Physics* 146 (1998), S. 322–345

[26] Guo, H. ; Smallwood, G. J.: The interaction between soot and NO formation in a laminar axisymmetric coflow ethylene/air diffusion flame. In: *Combustion and Flame* 149 (2007), S. 225–233

[27] Ivanova, E. ; Noll, B. ; Griebel, P. ; Aigner, M. ; Syed, K.: Numerical simulations of turbulent mixing and autoignition of hydrogen fuel at reheat combustor operating conditions. In: *Journal of Engineering for Gas Turbines and Power* 134 (2012), S. 041504–01–041504–07

[28] Jensen, E. J. ; Toon, O. B.: The potential impact of soot particles from aircraft exhaust on cirrus clouds. In: *Geophysical Research Letters* 24 (1997), S. 249–252

[29] Kärcher (ed.), B.: Particles and cirrus clouds / German Aerospace Center. 2008. – Forschungsbericht. – http://www.pa.op.dlr.de/pazi/DLR-Mitteilung_2008-01.pdf, accessed at December 17th, 2014

[30] Köhler, M. ; Geigle, K. P. ; Blacha, T. ; Gerlinger, P. ; Meier, W.: Experimental characterization and numerical simulation of a sooting lifted turbulent jet diffusion flame. In: *Combustion and Flame* 159 (2012), S. 2620–2635

[31] Lammel, O. ; Geigle, K. P. ; Lückerath, R. ; Meier., W. ; Aigner, M.: Investigation of soot formation and oxidation in a high-pressure gas turbine model combustor by laser techniques. In: *Proceedings of the ASME Turbo Expo 2007: Power for Land, Sea and Air*, 2007

[32] Lee, C. K.: Estimates of luminous flame radiation from fires. In: *Combustion and Flame* 24 (1975), S. 239–244

[33] Lefebvre, A. H.: Radiation from flames in gas turbines and rocket engines. In: *Proceedings of the Combustion Institute* 12 (1969), S. 1247–1253

[34] Leung, K. M. ; Lindstedt, R. P.: A simplified reaction mechanism for soot formation in nonpremixed flames. In: *Combustion and Flame* 87 (1991), S. 289–305

[35] Lindstedt, P. R.: Simplified soot nucleation and surface growth steps for non-premixed flames. In: Bockhorn, H. (Hrsg.): *Soot Formation in Combustion*. Springer Verlag, 1994

[36] Lindstedt, R. P. ; Waldheim, B. B. O.: Modeling of soot particle size distributions in premixed stagnation flow flames. In: *Proceedings of the Combustion Institute* 34 (2013), S. 1861–1868

[37] Lourier, M. ; Eberle, C. ; Noll, B. ; Aigner, M.: Influence of turbulence-chemistry interaction modeling on the structure and the stability of a swirl-stabilized flame. In: *Proceedings of the ASME Turbo Expo 2015: Power for Land, Sea and Air*, 2015

[38] McEnally, C. S. ; Pfefferle, L. D.: Experimental study of nonfuel hydrocarbons and soot in coflowing partially premixed ethylene air flames. In: *Combustion and Flame* 121 (2000), S. 575–592

[39] Menter, F. R.: Two-Equation Eddy-Viscosity Turbulence Models for Engineering Applications. In: *AIAA Journal* 32 (1994), S. 1598–1605

[40] Morgan, N. ; Kraft, M. ; Balthasar, M. ; Wong, D. ; Frenklach, M. ; Mitchell, P.: Numerical simulations of soot aggregation in premixed

laminar flames. In: *Proceedings of the Combustion Institute* 31 (2007), S. 693–700

[41] Mosbach, S. ; Celnik, M. S. ; Raj, A. ; Kraft, M. ; Zhang, H. R. ; Kubo, S. ; Kim, K.: Towards a detailed soot model for internal combustion engines. In: *Combustion and Flame* 156 (2009), S. 1156–1165

[42] Mueller, M. E. ; Pitsch, H.: Large eddy simulation of soot evolution in an aircraft combustor. In: *Physics of Fluids* 25 (2013), S. 110812

[43] Nakamura, M. ; Koda, S. ; Akita, K.: Sooting behavior and radiation in methanol/benzene/air diffusion flames. In: *Proceedings of the Combustion Institute* 19 (1982), S. 1395–1401

[44] Nicoud, F. ; Ducros, F.: Subgrid-scale stress modelling based on the square of the velocity gradient tensor. In: *Flow, Turbulence and Combustion* 62 (1999), S. 183–200

[45] Petzold, A. ; Ström, J. ; Ohlsson, S. ; Schröder, F. P.: Elemental composition and morphology of ice-crystal residual particles in cirrus clouds and contrails. In: *Atmospheric Research* 49 (1998), S. 21–34

[46] Petzold, A. ; Ström, J. ; Schröder, F. P. ; Kärcher, B.: Carbonaceous aerosol in jet engine exhaust: emission characteristics and implications for heterogeneous chemical reactions. In: *Atmospheric Environment* 33 (1999), S. 2689–2698

[47] Pope, C. J. ; Howard, J. B.: Simultaneous particle and molecule modeling (SPAMM): An approach for combining sectional aerosol equations and elementary gas-phase reactions. In: *Aerosol Science and Technology* 27 (1997), S. 73–94

[48] Pope, S. B.: Ten questions concerning the large eddy simulation of turbulent flows. In: *New Journal of Physics* 6 (2004), Nr. 35, S. 1–24

[49] Qamar, N. H. ; Alwahabi, Z. T. ; Chan, Q. N. ; Nathan, G. J. ; Roekaerts, D. ; King, K. D.: Soot volume fraction in a piloted turbulent jet nonpremixed flame of natural gas. In: *Combustion and Flame* 156 (2009), S. 1339–1347

[50] Richter, H. ; Granata, S. ; Green, W. H. ; Howard, J. B.: Detailed modeling of PAH and soot formation in a laminar premixed benzene/oxygen/argon low-pressure flame. In: *Proceedings of the Combustion Institute* 30 (2005), S. 1397–1405

[51] Saffaripour, M. ; Zabeti, P. ; Dworkin, S. B. ; Zhang, Q. ; Guo, H. ; Liu, F. ; Smallwood, G. J. ; Thomson, M. J.: A numerical and experimental study of a laminar sooting coflow Jet-A1 diffusion flame. In: *Proceedings of the Combustion Institute* 33 (2011), S. 601–608

[52] Saji, C. B. ; Balaji, C. ; Sundararajan, T.: Investigation of soot transport and radiative heat transfer in an ethylene jet diffusion flame. In: *International Journal of Heat and Mass Transfer* 51 (2008), S. 4287–4299

[53] Santoro, R. J. ; Yeh, T. T. ; Horvath, J. J. ; Semerjian, H. G.: The transport and growth of soot particles in laminar diffusion flames. In: *Combustion Science and Technology* 53 (1987), S. 89–115

[54] Slavinskaya, N. A. ; Frank, P.: A modelling study of aromatic soot precursors formation in laminar methane and ethene flames. In: *Combustion and Flame* 156 (2009), S. 1705–1722

[55] Slavinskaya, N. A. ; Haidn, O. J.: Reduced chemical model for high pressure methane combustion with PAH formation. In: *Proceedings of the 46th AIAA Aerospace Sciences Meeting*, 2008

[56] Smooke, M. D. ; Long, M. B. ; Connelly, B. C. ; Colket, M. B. ; Hall, R. J.: Soot formation in laminar diffusion flames. In: *Combustion and Flame* 143 (2005), S. 613–628

[57] Stöhr, M. ; Geigle, K. P. ; ; Meier, W.: *Correlated velocity and soot measurements in a gas turbine model combustor*. 2015. – Unpublished data. In preparation for publication

[58] Tsurikov, M. S. ; Geigle, K. P. ; Krüger, V. ; Schneider-Kühnle, Y. ; Stricker, W. ; Lückerath, R. ; Hadef, R. ; Aigner, M.: Laser-based investigation of soot formation in laminar premixed flames at atmospheric and elevated pressures. In: *Combustion Science and Technology* 177 (2005), S. 1835–1862

[59] Yunardi ; Woolley, R. M. ; Fairweather, M.: Conditional moment closure prediction of soot formation in turbulent, nonpremixed ethylene flames. In: *Combustion and Flame* 152 (2008), S. 360–376

[60] Zamuner, B. ; Dupoirieux, F.: Numerical simulation of soot formation in a turbulent flame with a monte-carlo PDF approach and detailed chemistry. In: *Combustion Science and Technology* 158 (2000), S. 407–438

[61] Zhao, B. ; Yang, Z. ; Li, Z. ; Johnsten, M. V. ; Wang, H.: Particle size distribution function of incipient soot in laminar premixed ethylene flames: effect of flame temperature. In: *Proceedings of the Combustion Institute* 30 (2005), S. 1441–1448